

Performance of a liquid nitrogen cryostat for the study of nuclear recoils in undoped CsI crystals

K. Ding, J. Liu, Y. Yang, K. Scholberg, D.M. Markoff

*Department of Physics, University of South Dakota,
414 East Clark Street, Vermillion, South Dakota 57069, USA*

E-mail: keyu.ding@coyotes.usd.edu

ABSTRACT: There is a global trend to increase the light yield of CsI scintillators used in neutrino and dark matter detection by operating undoped crystals at cryogenic temperatures. However, high light yield alone is not sufficient to guarantee a low energy threshold. The response of undoped crystals to nuclear recoils at cryogenic temperatures is equally important. A liquid nitrogen-based cryostat was developed to measure the nuclear quenching factor of a small undoped CsI crystal using monoenergetic neutron beams at the Triangle Universities Nuclear Laboratory (TUNL). To avoid neutron scattering in high- z materials, they were intentionally reduced around the crystal. The structure and performance of the cryostat are described in detail. Using this cryostat, a light yield of 33.4 ± 1.7 photoelectrons per keV electron-equivalent (PE/keV_{ee}) was observed at 5.9 keVee, enabling the measurement of nuclear quenching factors at very low energies. The results of the quenching factor measurement will be reported in a subsequent paper.

Non-negligible overshooting was observed in the tails of light pulses. The origin of this issue and the correction procedure are described in detail. This information may be useful for others who encounter similar technical challenges.

KEYWORDS: Cryogenic detectors, Inorganic scintillators, Overshooting correction, Dark Matter detectors, Non-standard neutrino interactions detector

ARXIV EPRINT: [1608.06278](https://arxiv.org/abs/1608.06278)

Contents

1	Introduction	1
2	Cryostats	2
2.1	Design based on gravity-fed liquid nitrogen dewar	2
2.2	Design based on open liquid nitrogen dewar	3
3	Single-photoelectron (SPE) response of the PMT	4
4	Energy calibration	6
4.1	Correction of overshooting	7
5	Light yield	8
6	Conclusion	9

1 Introduction

Undoped cesium iodide (CsI) at around liquid nitrogen temperature are very bright scintillating crystals [1–3]. When combined with photo-sensors working at cryogenic temperatures, the light yield of these crystals can be at least twice higher than that of Tl- or Na-doped CsI operated at room temperature [4]. The authors have systematically examined light yields of undoped CsI crystals from SICCAS, AMCRYS, and OKEN, with various sizes, from 13 keV To 2.6 MeV, directly coupled with PMTs or SiPMs at liquid nitrogen temperature [5–9]. The highest light yield obtained was 43.0 PE/keV_{ee}, achieved with a small crystal coupled to two SensL J-series SiPMs [9].

With such high light yields, the energy threshold of such a detector can be significantly lower than that of a doped CsI. A 14 kg Na-doped CsI detector was used by the COHERENT Collaboration to observe 134 ± 22 Coherent Elastic neutrino(ν)-Nucleus Scattering (CEvNS) events with two years of operation at the Spallation Neutron Source (SNS), Oak Ridge National Laboratory (ORNL) [4]. Assuming a similar configuration and exposure, nearly 2,000 CEvNS events can be detected with an undoped CsI detector operated at liquid nitrogen temperature, thanks to its high light yield. Sensitivities of such a detector for probing non-standard neutrino interactions [10–17] and low-mass dark matter particles [18–25] at the Spallation Neutron Source (SNS), Oak Ridge National Laboratory (ORNL) are discussed in detail in Ref. [6, 8].

Those sensitivity studies were based on the assumption that undoped crystals at 77 K have a similar nuclear scintillation quenching effect to undoped ones at room temperature. A recent study at 108 K [26] seemly confirmed this assumption. However, measurements done with α particles [27] revealed strong temperature dependence of the quenching effect. It is hence important to measure the nuclear quenching effort closer to 77 K.

The nuclear quenching measurement is normally done by putting the material under study in a neutron beam. The energy of the nuclear recoil can then be calculated from the energy of the incident neutron and the angle of the scattered neutron, assuming the neutron

only scatters once within the target. High z material should hence be avoided around the target to minimize the occurrence of neutron multiple scatterings.

A liquid nitrogen cryostat with low- z material around a small undoped CsI crystal was developed for the nuclear quenching measurement. Its performance was compared to another cryostat previously used for light yield measurements.

A constant light yield was assumed in those sensitivity calculations. It is known, however, that the light yield of undoped CsI has non-negligible variations at different energy ranges, and it varies with crystals under investigation [28–30]. It is hence necessary to verify that the light yields we achieved from 13 keV to 2.6 MeV still hold at lower energies with our crystals purchased from Japan and Ukraine. A ^{55}Fe source and an ^{241}Am source were used to achieve this utilizing the 5.9 keV x -rays and 60 keV γ -rays.

2 Cryostats

2.1 Design based on gravity-fed liquid nitrogen dewar

Fig. 1 shows the experimental setup for the measurement of the light yield of an undoped CsI crystal at around 77 K. As seen in the right figure, liquid N_2 can drip from a dewar into a hollow pipe that is directly in contact with structures to be cooled. In the detector mounting mode, as shown in the left figure, the dewar can be taken away and this new cryostat can be flipped over, and placed into a dry glove box for crystal mounting. The middle figure is the CAD drawing of the cryostat and the right picture shows the overall experimental setup.

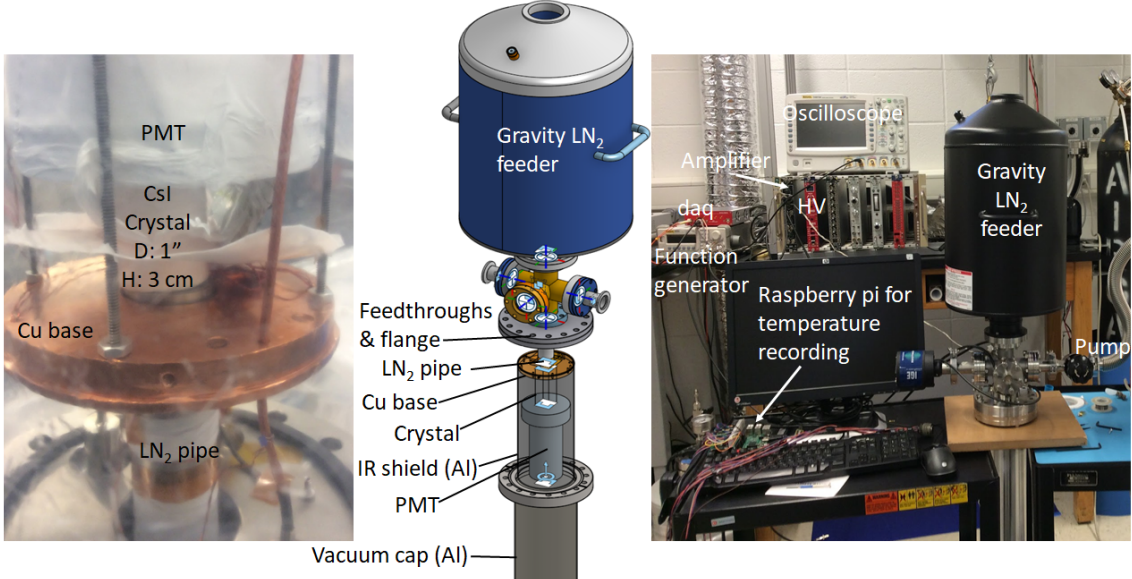


Figure 1. A sketch and pictures of the cryostat setup.

The undoped cylindrical crystal was purchased from AMCRYST [31], and had a diameter of 1 inch and a height of 3 cm. All surfaces were mirror polished. The side surface and an end side surface of the crystal were wrapped with multiple layers of Teflon tapes to make sure that there was no light leak. A Hamamatsu 3-inch R11069-ASSY PMT was pushed against the other end surface of the crystal by springs to ensure adequate optical contact without optical grease. The springs are held by the copper base. The wrapped end surface

of the crystal was pushed against the cooling finger of the cryostat where liquid nitrogen was fed into the LN₂ pipe.

To control a reasonable radiation intensity, an ²⁴¹Am source and a ⁵⁵Fe source were facing opposite towards the center of the crystal. Noted, 2 layers (0.032 mm) of aluminum foil were put on the ⁵⁵Fe source to further reduce the radiation intensity. The sources were attached to the inner side surface of the aluminum chamber (IR shield) in the cryostat.

To minimize exposure of the crystal to atmospheric moisture, assembly was done in a glove bag flushed with dry nitrogen gas. The relative humidity was kept below 10% at 22°C during the assembly process.

The PMT-crystal assembly was capped by an IR shield that was fixed to the copper base by three screws. The cryostat was then sealed by the vacuum cap to a 6-inch ConFlat (CF) flange. A fluorocarbon CF gasket was put in between for multiple operations. The inner diameter of the cryostat was ~ 10 cm. Vacuum welded to the flange were two BNC, two SHV, one 19-pin electronic feedthroughs.

After all cables were fixed beneath it, the top flange was closed. The chamber was then pumped with a Pfeiffer Vacuum HiCube 80 Eco to $\sim 1 \times 10^{-5}$ mbar. The feeder was then filled with LN₂ to cool the LN₂ pipe then further cool everything inside. The pump was on all the time until the end of the experiment.

A few Heraeus C 220 platinum resistance temperature sensors were used to monitor the cooling process. They were attached to the side surface of the crystal, the PMT, and the top flange to obtain the temperature profile of the long chamber. A Raspberry Pi 2 computer with custom software [32] was used to read out the sensors. The cooling process took about 10 hours. Most measurements, however, were taken after about 12 hours of waiting to let the system reach thermal equilibrium.

The PMT was powered by a CAEN N1470A high voltage power supply in a NIM crate. The signals were fed into a CAEN DT5751 waveform digitizer, which had a 1 GHz sampling rate, a 1 V dynamic range and a 10 bit resolution. WaveDump [33], a free software provided by CAEN, was used for data recording. The recorded binary data files were converted to CERN ROOT files for analysis by a custom-developed software [34].

2.2 Design based on open liquid nitrogen dewar

It is hard to measure the exact temperature of the crystal attached to the liquid nitrogen pipe without adding additional temperature sensors around it. To ensure that the crystal was operated at 77 K, we compared the light yield of crystal operated in the new cryostat with that operated in another cryostat. The structure of the latter is shown in Fig. 2. As the crystal is fully submerged in liquid nitrogen in this cryostat, its temperature is exactly 77 K. If the light yields measured in the two are similar, the crystals should have been operated at similar temperatures.

The detailed description of the old cryostat can be found in Ref. [7]. Other than two different cryostats being used in the two setups, one difference is the crystal. An undoped cylindrical crystal with a diameter of 2 inches and a height of 1 cm purchased from OKEN [35] was used in the old setup. The other difference is the radiation intensity as shown in the right Fig. 2, the old setup has a 1 mm copper in between the ²⁴¹Am and the crystal, and 2 more layers of aluminum foil in between the ⁵⁵Fe and the crystal. The sources are directly attached to the surface of the PTFE tape wrapping.

The same analysis was made on two setups. For convenience, only analysis from the new setup was shown.

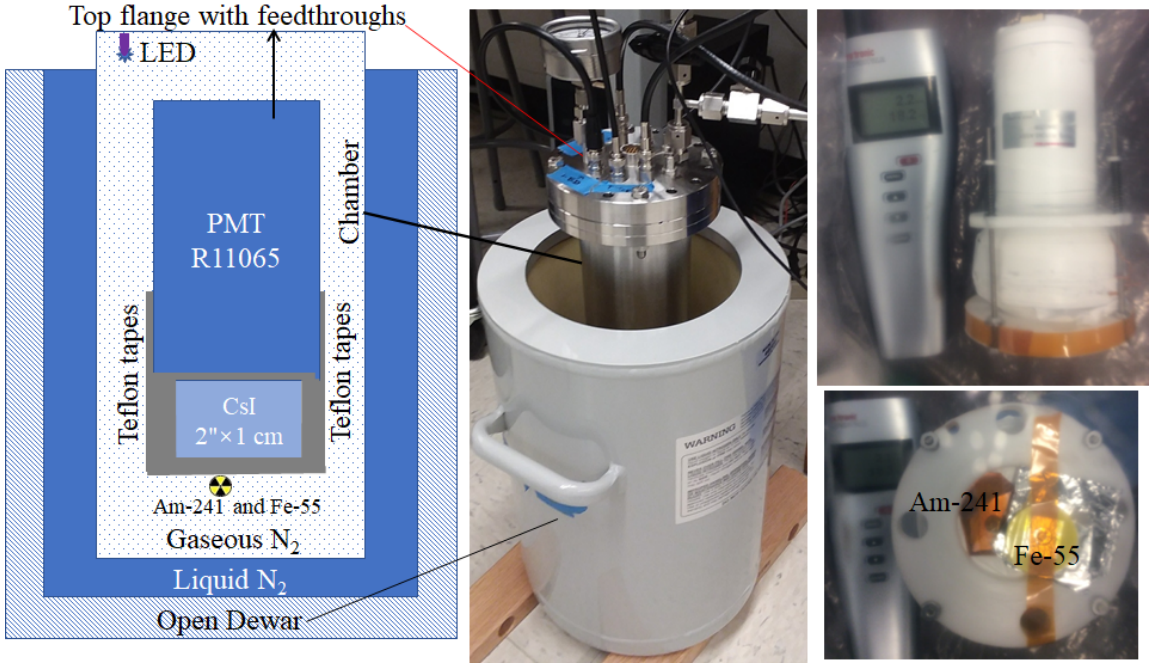


Figure 2. A sketch and pictures of the cryostat setup.

3 Single-photoelectron (SPE) response of the PMT

The SPE response of the PMT was measured using light pulses from an ultraviolet LED, LED370E from Thorlabs. Its output spectrum peaked at 375 nm with a width of 10 nm, which was within the 200 – 650 nm spectral response range of the PMT. Light pulses with a \sim 50 ns duration and a rate of 10 kHz were generated using an RIGOL DG1022 arbitrary function generator. The intensity of light pulses was tuned by varying the output voltage of the function generator so that only one or zero photon hit the PMT during the LED lit window most of the time. A TTL trigger signal was emitted from the function generator simultaneously together with each output pulse. It was used to trigger the digitizer to record the PMT response.

The PMT was biased at 1,600 V, slightly above the recommended operation voltage, 1,500 V, to increase the gain of the PMT. Single-PE pulses were further amplified by a factor of ten using a Phillips Scientific Quad Bipolar Amplifier Model 771 before being fed into the digitizer in order to separate them from the pedestal noise.

The left plot on Fig. 3 shows \sim 200 randomly selected waveforms from the PMT response of the SPE measurement. Some quality criteria were applied to filter out noise events. Firstly, the baseline was calculated in the following steps. The values corresponding to each sample (height) were added to a summed value, then an averaged value (baseline value) was calculated using the summed value divided by the number of samples. The baseline value was then used to shift the waveforms to zero by deducting this baseline value from each corresponding height value. Secondly, the root mean square (RMS) of the baseline was also calculated. Lastly, baseline values and RMS values of the baseline were calculated in a region of 0 to 100 ns, 200 to 300 ns and 400 to 500 ns. After that, baseline values and RMS values were set to be smaller than 1 ADC count. Another restriction is that the lowest height of the waveform should be bigger than -2 ADC counts. Eventually,

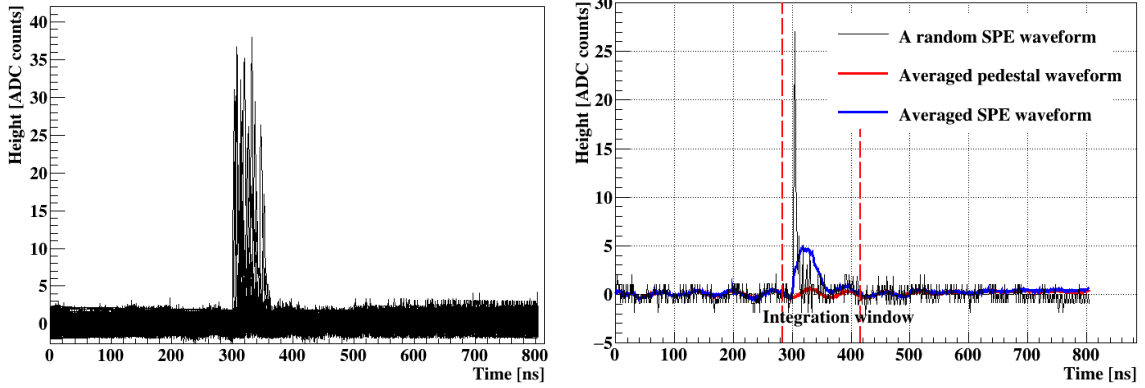


Figure 3. Left: 196 selected waveforms from the PMT overlapped with each other. Right: A random SPE waveform, averaged SPE waveform and averaged pedestal waveform.

196 SPE waveforms were selected applying those restrictions to 1300 SPE events. However, some fluctuations still exist in the pedestal which also sit under the SPE waveforms.

To examine the influence of the unstable pedestal on the SPE waveform, the averaged pedestal waveform was drawn in the right plot on Fig. 3. The averaged SPE waveform was also drawn to discover its correlation with the averaged pedestal waveform; the baseline and averaged SPE coincided with each other except in the region where SPE responds. Therefore, the mean area of the SPE can be obtained by subtracting the area of the averaged pedestal waveform from the area of the averaged SPE waveform. The integration window starts from and ends on both pulses crossing zero as shown in the plot. However, SPE waveforms were seen to have much higher heights in the left plot, yet the averaged SPE waveform only has a height of ~ 5 ADC counts in the right plot. To investigate the discrepancy, we randomly selected an SPE waveform, which was much narrower than the averaged waveform. The wider width of the averaged waveform was due to the fact that the SPE pulses appeared at different locations, ranging from approximately 300 to 360 ns.

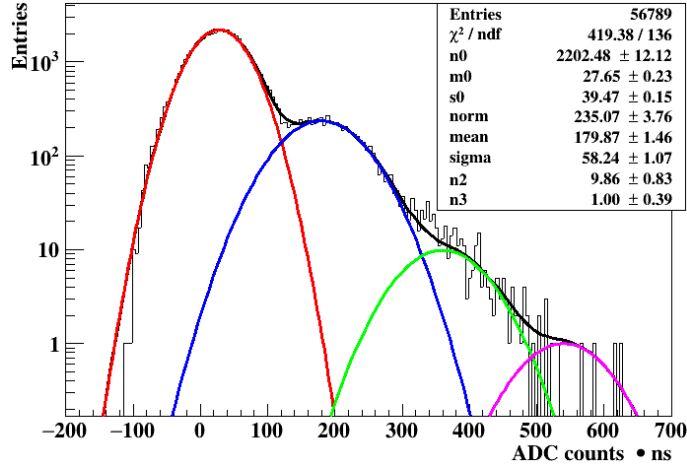


Figure 4. SPE response of the PMT in logarithm scale.

The integration window (283-416 ns) shown in the right plot in Fig. 3 and the same cuts applied to the selected waveforms were then used for each waveform in the data file.

The resulting SPE spectrum is shown in Fig. 4. The spectrum was fitted in the same way as described in Ref. [7, 36]. Where the red Gaussian curve is fitted for the pedestal events, the blue Gaussian curve is fitted for the SPE events, two PE fitting (green curve) and three PE fitting (pink curve) were Gaussian functions based on the mean and sigma obtained from the SPE fitting. The black curve is the sum of those fittings, which well matches the single PE response. The area of single PE (mean_{SPE}) would be, as mentioned in the third sentence in the last paragraph, $\text{mean}_{\text{SPE}} = \text{mean} - m_0$, where mean and m_0 are obtained from the fitting result in Fig. 4. The value of mean_{SPE} is 152.22 ADC counts·ns, and the value of m_0 is 27.65 ADC counts·ns, they will be further used in the light yield calculation.

4 Energy calibration

The energy calibration was performed using a ^{55}Fe source and an ^{241}Am source. The digitizer was triggered when the height of a pulse from the PMT was more than 50 ADC counts (~ 2 PE). As can be seen in Fig. 3, the height of a single PE pulse was around 25 ADC counts, the trigger threshold could hence suppress most of the electronic noise spikes while letting pass most of the PE pulses. The trigger rate was ~ 2.3 kHz when the threshold was set to this value.

Each recorded waveform was 10000 ns long as shown in Fig. 5. About 1000 ns pre-traces were preserved before the rising edge of a pulse that triggered the digitizer so that there were enough samples before the pulse to calculate the averaged pedestal value of the waveform, and 200 samples starting from zero were used to calculate the baseline. The pedestal was then adjusted to zero.

By checking a few waveforms, overshooting was commonly observed. To further identify whether overshooting was common to see, averaged waveforms were drawn. As shown in Fig. 5, averaged pulses were drawn, by summing all the waveforms first, then dividing by the number of events. The tallest one is the averaged 59.5 keV waveform, the second tallest one is the averaged 26.3 keV waveform, the second smallest one is the averaged 17.5 keV waveform, and the smallest one is the averaged 5.9 keV waveform. In the left figure, the overshooting effect from the PMT was clearly seen.

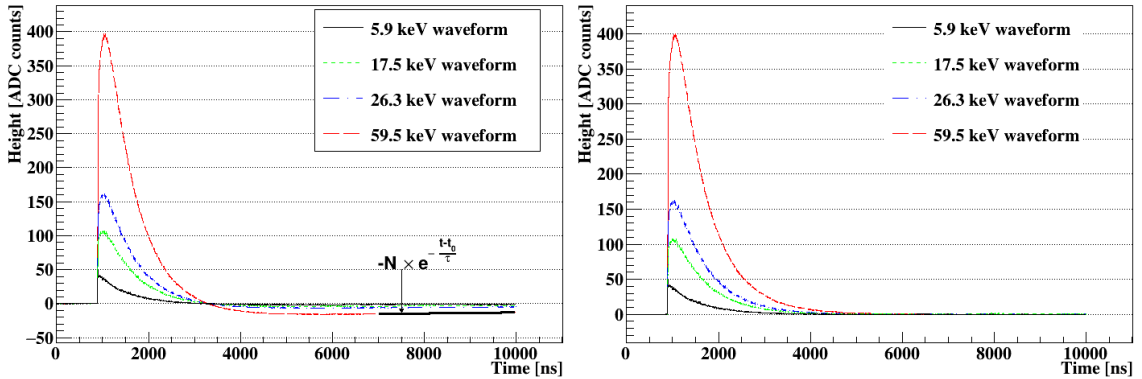


Figure 5. Left: Averaged waveforms with overshooting. The tail part of the waveform was fitted by an exponential function to estimate the overshooting effect. Right: Averaged waveforms after correction.

4.1 Correction of overshooting

Fig. 6 shows the high voltage (HV) distribution circuit and the readout scheme of our PMT given by its manufacturer, Hamamatsu Photonics K.K. A 2,000 pF capacitor, C , is used to decouple the output line from the anode biased at a high voltage. The 51 Ohm load resistor, R , is used to match the impedance of typical oscilloscopes and digitizers. The waveform of V_{out} can be tuned by selecting the values of C, C', R , and R' as described in detail in Ref. [37]. We did not observe overshooting in previous measurements when we used the same PMT. The values of these passive components must have been fine-tuned by Hamamatsu to reduce overshooting. However, their values may have changed over time and through multiple thermal cycles, which resulted in the overshooting shown in Fig. 5.

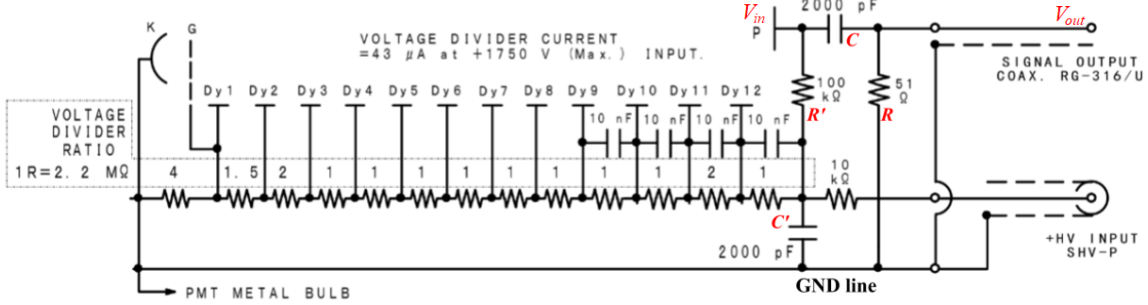


Figure 6. Circuit from Hamamatsu.

As the RC circuit is the origin of the overshoot, it is possible to correct this effect offline. A simple numerical method was developed to achieve this. Its derivation is explained step by step here. First, the current going through the load resistor R can be expressed as

$$I = \frac{V_{out}}{R} = \frac{dQ}{dt}, \quad (4.1)$$

where Q is the charge accumulated in C . It can be expressed as

$$Q = C(V_{in} - V_{out}). \quad (4.2)$$

Combine the two equations, we have

$$\frac{dQ}{dt} = C\left(\frac{dV_{in}}{dt} - \frac{dV_{out}}{dt}\right) = \frac{V_{out}}{R}, \quad (4.3)$$

which can be rearrange as

$$V_{out} = RC\left(\frac{dV_{in}}{dt} - \frac{dV_{out}}{dt}\right) \quad (4.4)$$

Numerically, this can be written as

$$V_{out}[i] = RC\left(\frac{V_{in}[i] - V_{in}[i-1]}{\Delta t} - \frac{V_{out}[i] - V_{out}[i-1]}{\Delta t}\right), \quad (4.5)$$

where i is the index of individual samples in the waveform, and $\Delta t = 1$ ns is the time interval between two consecutive samples. The iterative expression of V_{in} can be derived from Eq. 4.5:

$$V_{in}[i] = \frac{RC + \Delta t}{RC}V_{out}[i] - V_{out}[i-1] + V_{in}[i-1]. \quad (4.6)$$

The RC constant in Eq. 4.6 was measured to be 18,044 ns by fitting a simple exponential function to the averaged waveforms as shown in Fig. 5 in the range of [7,000, 10,000] ns, where the influence of scintillation decay can be neglected and the influence of the RC circuit persists.

Therefore, V_{out} can be corrected back sample by sample once the RC constant was identified. The averaged waveforms after correction shown in the right Fig. 5 demonstrate the success of this correction method and the rationality of the RC constant. The same correction method with the same RC constant was then applied to each waveform and gave us reasonable waveforms.

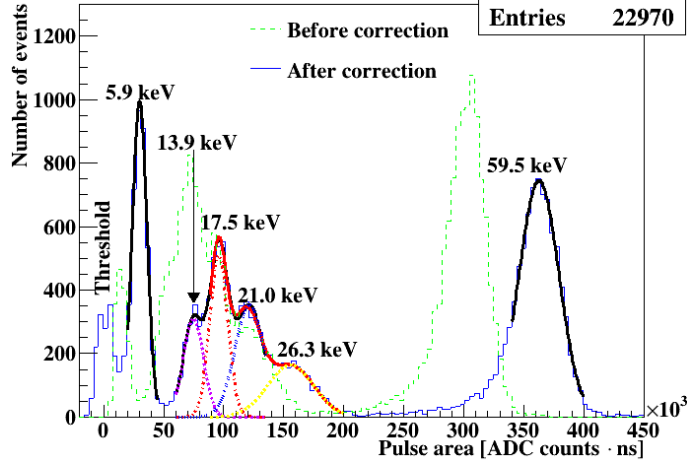


Figure 7. Energy spectra of ^{55}Fe and ^{241}Am in the unit of ADC counts·ns.

Every waveform after the correction was integrated from zero to the end. The integration had a unit of ADC counts·ns. In Fig. 7, the recorded energy spectra before correction is the green dashed line histogram, the energy spectra after correction is the blue solid line histogram. A dominant 5.9 keV peak from ^{55}Fe can be seen, 17.5 keV, 26.3 keV and 59.5 keV peaks from ^{241}Am are shown as well. Fits were applied to the corrected spectra. The Gaussian fit was applied to the 5.9 and 59.5 keV peaks, the combined fit was applied to 13.9, 17.5 and 21.0 keV peaks, then applied to 17.5, 21.0 and 26.3 keV peaks. Pulses area mean obtained from those fits were summarized in Table 1, and whether the light response stays consistent in the energy closing to the threshold was compared later.

5 Light yield

The pulse area values (A) of the radiation pulses in the unit of ADC counts·ns were converted to the number of PE (N_{PE}) using the formula:

$$N_{\text{PE}} = \frac{A - m_0}{\text{mean}_{\text{SPE}}}. \quad (5.1)$$

The shift value, m_0 , is added to account for the overall shift of the pulses observed in the single PE measurement. However, compared to the pulse area values, it is much smaller, adding it to the equation does not change the final result much.

The light yield (Y) for a given energy deposited (E_{dep}) in our electron recoil measurements was then calculated using the following equation:

$$Y \text{ [PE/keV}_{\text{ee}}\text{]} = \frac{N_{\text{PE}}}{E_{\text{dep}}}. \quad (5.2)$$

Table 1. Fitting results along with the calculated light yield of ^{59}Fe and ^{241}Am peaks in the energy spectrum are shown. The top table is from the new cryostat, whereas the bottom table is from the old cryostat.

Type of radiation	Energy [keV _{ee}]	Mean (A) [ADC·ns]	Sigma [ADC·ns]	FWHM %	Light yield [PE/keV _{ee}]
X-ray	5.9	29984	6138	48.2	33.4
X-ray	13.9 [†]	74709	8330	26.3	35.3
X-ray	17.5 [†]	95885	7516	17.8	36.0
X-ray	21.0 [†]	121409	12000	23.3	38.0
γ -ray	26.3 [†]	155757	19322	29.2	38.9
γ -ray	59.5	362693	16607	10.8	40.0

Type of radiation	Energy [keV _{ee}]	Mean (A) [ADC·ns]	Sigma [ADC·ns]	FWHM %	Light yield [PE/keV _{ee}]
X-ray	5.9	32261	5454	39.8	35.9
γ -ray	26.3	166507	14310	20.2	41.6
γ -ray	59.5	354948	13264	8.8	39.2

[†] Intensity averaged mean of X-rays near each other [7].

In the new cryostat, the light yield from the 5.9 keV radiation is 33.4 ± 1.7 PE/keV_{ee}, while the light yield from the 59.5 keV radiation is 40.0 ± 2.0 PE/keV_{ee}. The variation in the light yield at different energies is also seen in the old cryostat setup, with a light yield of 35.9 ± 1.8 PE/keV_{ee} from the 5.9 keV radiation and a light yield of 39.2 ± 2.0 PE/keV_{ee} from the 59.5 keV radiation. One thing worth noting is the similar light yields observed from two cryostats, confirming the cooling capability of the new cryostat.

6 Conclusion

This study describes the development of a liquid nitrogen-based cryostat for measuring the nuclear quenching factor of undoped CsI crystals at cryogenic temperatures. The cryostat was designed to avoid neutron scattering in high- z materials and achieved a light yield of 33.4 ± 1.7 PE/keV_{ee} at 5.9 keV_{ee}. The results of the quenching factor measurement will be reported in a subsequent paper. Additionally, the study highlights the issue of non-negligible overshooting in the tails of light pulses and provides a detailed explanation of its origin and correction procedure. The information presented in this study will be valuable for others working in similar fields and encountering similar technical challenges.

Acknowledgments

This work is supported by the Department of Energy (DOE), USA, award DE-SC0022167, and the National Science Foundation (NSF), USA, award PHY-1506036. Computations

supporting this project were performed on High Performance Computing systems at the University of South Dakota, funded by NSF award OAC-1626516.

References

- [1] H. Nishimura, M. Sakata, T. Tsujimoto and M. Nakayama, *Origin of the 4.1-eV luminescence in pure CsI scintillator*, *Phys. Rev. B* **51** (1995) 2167–2172.
- [2] C. Amsler, D. Grögler, W. Joffrain, D. Lindelöf, M. Marchesotti, P. Niederberger et al., *Temperature dependence of pure CsI: scintillation light yield and decay time*, *Nucl. Instrum. Meth. A* **480** (2002) 494–500.
- [3] C. Sailer, B. Lubsandorzhiev, C. Strandhagen and J. Jochum, *Low temperature light yield measurements in NaI and NaI(Tl)*, *Europ. Phys. J. C* **72** (2012) 2061.
- [4] C. Collaboration, D. Akimov et al., *Observation of coherent elastic neutrino-nucleus scattering*, *Science* (2017) eaao0990.
- [5] J. Liu, M. Yamashita and A. K. Soma, *Light yield of an undoped CsI crystal coupled directly to a photomultiplier tube at 77 Kelvin*, *J. Inst.* **11** (2016) P10003.
- [6] D. Chernyak, D. Pershey, J. Liu, K. Ding, N. Saunders and T. Oli, *Prospect of undoped inorganic crystals at 77 kelvin for low-mass dark matter search at spallation neutron source*, *Eur. Phys. J. C* **80** (2020) 547.
- [7] K. Ding, D. Chernyak and J. Liu, *Light yield of cold undoped CsI crystal down to 13 keV and the application of such crystals in neutrino detection*, *Eur. Phys. J. C* **80** (2020) 1146.
- [8] K. Ding, D. Pershey, D. Chernyak and J. Liu, “Prospect of undoped inorganic scintillators at 77 Kelvin for the detection of non-standard neutrino interactions at the Spallation Neutron Source.” 2020.
- [9] K. Ding, J. Liu, Y. Yang and D. Chernyak, *First operation of undoped CsI directly coupled with SiPMs at 77 K*, *Eur. Phys. J. C* **82** (2022) 344.
- [10] S. Davidson, C. P. na Garay, N. Rius and A. Santamaria, *Present and future bounds on non-standard neutrino interactions*, *Journal of High Energy Physics* **2003** (2003) 011.
- [11] J. Barranco, O. G. Miranda and T. I. Rashba, *Probing new physics with coherent neutrino scattering off nuclei*, *J. High Energy Phys.* **2005** (2005) 21.
- [12] P. Coloma and T. Schwetz, *Generalized mass ordering degeneracy in neutrino oscillation experiments*, *Phys. Rev. D* **94** (2016) 055005.
- [13] P. Coloma et al., *Curtailing the dark side in non-standard neutrino interactions*, *JHEP* **2017** (2017) 116.
- [14] J. Liao and D. Marfatia, *COHERENT constraints on nonstandard neutrino interactions*, *Physics Letters B* **775** (2017) 54–57.
- [15] D. K. Papoulias and T. S. Kosmas, *COHERENT constraints to conventional and exotic neutrino physics*, *Phys. Rev. D* **97** (2018) 033003.
- [16] P. B. Denton, Y. Farzan and I. M. Shoemaker, “A Plan to Rule out Large Non-Standard Neutrino Interactions After COHERENT Data.” 2018.
- [17] P. S. B. Dev et al., “Neutrino Non-Standard Interactions: A Status Report.” 2019.
- [18] I. Kobzarev, L. Okun and I. Pomeranchuk, *On the possibility of experimental observation of mirror particles*, *Sov. J. Nucl. Phys.* **3** (1966) 837–841.
- [19] S. I. Blinnikov and M. Yu. Khlopov, *ON POSSIBLE EFFECTS OF 'MIRROR' PARTICLES*, *Sov. J. Nucl. Phys.* **36** (1982) 472.

- [20] R. Foot, H. Lew and R. R. Volkas, *A model with fundamental improper spacetime symmetries*, *Phys. Lett. B* **272** (1991) 67–70.
- [21] H. M. Hodges, *Mirror baryons as the dark matter*, *Phys. Rev. D* **47** (1993) 456–459.
- [22] Z. G. Berezhiani, A. D. Dolgov and R. N. Mohapatra, *Asymmetric inflationary reheating and the nature of mirror universe*, *Phys. Lett. B* **375** (1996) 26–36.
- [23] B. Lee and S. Weinberg, *Cosmological lower bound on heavy-neutrino masses*, *Phys. Rev. Lett.* **39** (Jul, 1977) 165–168.
- [24] E. Izaguirre, G. Krnjaic, P. Schuster and N. Toro, *Analyzing the Discovery Potential for Light Dark Matter*, *Phys. Rev. Lett.* **115** (2015) 251301, [[1505.00011](#)].
- [25] P. Fayet, *Extra $U(1)$ ’s and new forces*, *Nucl. Phys. B* **347** (1990) 743–768.
- [26] C. M. Lewis and J. I. Collar, *Response of undoped cryogenic CsI to low-energy nuclear recoils*, *Physical Review C* **104** (July, 2021) 014612.
- [27] M. Clark, P. Nadeau, S. Hills, C. Dujardin and P. C. F. Di Stefano, *Particle detection at cryogenic temperatures with undoped CsI*, *Nuclear Instruments and Methods in Physics Research Section A: Accelerators, Spectrometers, Detectors and Associated Equipment* **901** (Sept., 2018) 6–13.
- [28] M. Moszyński, M. Balcerzyk, W. Czarnacki, M. Kapusta, W. Klamra, P. Schotanus et al., *Energy resolution and non-proportionality of the light yield of pure CsI at liquid nitrogen temperatures*, *Nuclear Instruments and Methods in Physics Research Section A: Accelerators, Spectrometers, Detectors and Associated Equipment* **537** (Jan., 2005) 357–362.
- [29] S. S. Gridin, A. N. Belsky, N. V. Shiran and A. V. Gekhtin, *Channels of Energy Losses and Relaxation in CsI*, *IEEE Transactions on Nuclear Science* **61** (Feb., 2014) 246–251.
- [30] S. Kerisit, K. M. Rosso, B. D. Cannon, F. Gao and Y. Xie, *Computer simulation of the light yield nonlinearity of inorganic scintillators*, *Journal of Applied Physics* **105** (June, 2009) 114915.
- [31] “AMCRYS.”
- [32] J. Mammo, *Josephss/CraViS*, 2018.
- [33] “WaveDump - CAEN Digitizer readout application.”
- [34] J. Liu, *jintonic/toward*, 2021.
- [35] “OKEN -OHYO KOKEN KOGYO CO., LTD..”
- [36] T. Alexander et al., *Light yield in DarkSide-10: A prototype two-phase argon TPC for dark matter searches*, *Astropart. Phys.* **49** (2013) 44–51.
- [37] F. J. Luo, Y. K. Heng, Z. M. Wang, P. L. Wang, Z. H. Qin, M. H. Xu et al., *PMT overshoot study for JUNO prototype detector*, *Chinese Physics C* **40** (Sept., 2016) 096002.